Electronic Supplementary Information (ESI)

Chloride Transport in Conductive Polymer Films for an n-Type Thermoelectric Platform

Byeonggwan Kim, Jong Un Hwang, and Eunkyoung Kim*

Department of Chemical and Biomolecular Engineering, Yonsei University, 50 Yonsei-ro, Seodaemun-gu, Seoul 03722, South Korea

E-mail: *Prof. E. Kim, eunkim@yonsei.kr

Materials, methods, and characterization

Materials

AI4083 (solid content of 1.5 wt%) was purchased from Heraeus Clevios™. Copper (II) chloride, double-walled carbon nanotubes (DWCNTs) and 1-(ethoxycarbonylmethyl)-6-methoxyquinolinium bromide (MQAE) were purchased from Sigma-Aldrich Korea. Cerasolzer #186 (indium wire) was purchased from Kuroda Electric Co. LTD. Purified arc-discharge single-walled carbon nanotubes (SWCNTs) produced at Hanwha Nanotech, Grade ASP-100F, were used as received. Monolayer graphene on PET film (size: 1" × 1") was purchased from the Graphene Supermarket. Indium-tin oxide (ITO) glass (7 Ω/sq. resistivity) was purchased from Wooyang GMS, Co. Ltd.

Confocal microscopy

PEDOT:PSS and NPC40 solutions were prepared, and MQAE was added at 0.5wt% as a chlorine indicator.[1] The solution was drop-cast onto a cleaned slide glass (area of 1.5 × 0.7 cm^2) with a polyimide spacer of 300 μm thickness and dried in ambient conditions (~24 °C and ~50% RH) for 6 h. Then, the other cleaned slide glass was put on the spacer to make a sandwich-type sample at 90% RH. This sample was placed vertically on a cleaned slide glass, and Peltier modules attached to the heat sink linked by a thermal paste were contacted on both sides. The temperature gradient was controlled by applying an input current of +0.5 or −0.5 A. A confocal microscope (LSM 880, Carl Zeiss) was used for obtaining images of the side view. A 405 nm wavelength laser was used as the excitation source for MQAE.

MQAE was used as the Cl^- indicator (via diffusion-limited collisional quenching) according to the following quenching reaction (Equations S1-3):

$MQAE + hv \rightarrow MQAE^*$ (Equation S1)

$MQAE^* \rightarrow MQAE + hv$ (Equation S2)

$MQAE^* + Cl^- \rightarrow MQAE + Cl^{-*}$ (Equation S3)

NMR study

To prove the metal ion interaction with PSS in the NPC media, ^{1}H NMR spectra was performed in D_2O as a deuterated solvent (Fig. S5). Three broad peaks were measured; a and b present the backbone protons of PSS, and c and d present the phenyl ring protons of PSS (Fig. S5a). Specifically, peak d is shifted to a higher frequency from 7.47 to 7.66 ppm as the Cu^{2+} concentration increases because when the Cu^{2+} ion ionically cross-links with PSS^-, it withdraws electron density from PSS^-, mainly from the phenyl ring protons.[2] Because the proton at d is located on the solvent side rather than the protons at c due to the hydrolysis of sulfonate group in D_2O, peak d is broadened as the gelation progresses far from the solvent. Interestingly, the sharp peak of PEDOT shifted slightly at 3.61 ppm for NPC samples (Fig. S5b). The ^{1}H-NMR spectrum was obtained using a BRUKER ARX-400 spectrometer. In general, 0.5 mL of PEDOT:PSS or NPC solutions were dried on a slide glass at 20–25 °C and ~50% RH for 12 h and redispersed in D_2O (0.5 mL) as a deuterated solvent.

Characterization

The Seebeck voltage and temperature gradient were determined from a homemade setup using an Agilent 34410A Multimeter and Agilent 34970A, respectively.[3, 4] For the general measurement, two Peltier devices attached to an aluminum heat sink linked by a thermal paste (~4 mm apart) were used to generate the temperature gradient. The temperature gradient was controlled by applying various input currents, from +0.5 to −0.5 A, on the two Peltier devices using a Keithley 2400 Multimeter. The temperature gradient along the gap of the electrodes was determined by two T-type thermocouples on the z-direction controllable stage. The average saturated temperature was measured by the two thermocouples from the hot and cold electrodes at room temperature. The temperature difference in the samples was cross-checked by using a high-resolution IR camera (FLIR E40) and control programmed software in a dark room at room temperature, which was set to 23−25 °C with an error of 0.2 °C, for clear analysis. The voltage difference was obtained at the same points (electrodes) to minimize error. The temperature sensitivity of the thermocouple was 0.001 °C. The humidity in the Seebeck voltage measurement system was controlled by the volume of deionized water in the sealed chamber and was directly measured by a hygrometer (sensitivity of 1% RH). The Seebeck voltage of the device was measured after 30 min saturation and stabilization at a specific humidity. To confirm the Seebeck coefficient, six ΔV and ΔT points were determined 3 times each with various source currents, and the ΔV values were plotted linearly against ΔT.

The cyclic voltammograms, galvanostatic charge-discharge curves, and electrochemical impedance spectroscopy were performed at room temperature using an electrochemical interface and impedance analyzer (COMPACTSTAT, IVIUM technology). The electrochemical performances of the samples (0.7 cm × 0.7 cm) were obtained using a 2-electrode setup. An active area of ~0.21 cm^2 was tested under different RH values at 23 °C.

The film morphology and energy-dispersive X-ray spectroscopy (EDS) mapping images were obtained with a field emission scanning electron microscope (FE-SEM, JSM-7100F, JEOL Korea Ltd.). After fully drying the NPC solution on ITO glass, Pt sputtering was performed on the sample for 120 s at 10 mA.

Time-of-flight secondary ion mass spectrometer (ToF-SIMS) mapping was performed on the cross-section surface by TOF SIMS 5 (ION TOF GmbH, Münster, Germany) with a 30 keV Bi_1 primary beam. The diameter of the aperture was set to 100 μm. During the measurement, a 0.5 pA Bi_1 primary beam with a nominal diameter of 80 nm was rastered over the measurement area. The analyzed mass were 35 Cl^-, giving images of distributions of chlorine in the measured area. The scan was repeated for ~10 min. Mass spectra from 200 × 200 μm^2 areas were taken with Bi_3^+ in negative polarity using a 0.38 pA primary beam.

Transmission electron microscopy (TEM) and electron diffraction pattern were performed by JEM-F200, JEOL Korea Ltd. 5 μL of NPC solution was drop-casted on a carbon film-coated TEM Cu grid (200 mesh) and spin-coated at 1500 rpm for 30 s. It was dried at 60 °C for 10 min prior to the measurement. The gelled particle sizes were 33±2 nm, 240±14 μm, to 570±40 μm for NPC14, NPC25, and NPC40, respectively. Only the NPC57 film showed a crystalline electron diffraction pattern, especially the (210) crystalline plane of $CuCl_2$, with unknown patterns.

The film morphology was observed by atomic force microscopy (AFM, XE-100, Park Systems). All NPC solutions were drop-casted onto graphene film (40 $\mu L\ cm^{-2}$) and dried for 2 h in ambient conditions. The thickness of the films was measured by an Alpha step profilometer (Tencor Instruments, Alpha-step IQ).

UV-vis-NIR spectra (Lambda 750, UV/Vis/NIR Spectrophotometer, PerkinElmer) of the devices (thickness of 35 μm) were measured. Fluorescence spectra were obtained with a luminescence spectrometer (Perkin Elmer, Model LS55). Then, 50 μL of the sample solution was mixed with 4 mL of deionized water for dilution. MQAE (0.5 wt% solid content) was added to the solution.

High-resolution X-ray diffraction (HR-XRD) patterns were recorded on a SmartLab, Rigaku using CuKα radiation (λ=0.154 nm) at 9 kW beam power and a step size of 0.02 ° at a scan speed of 3 ° min^{-1}. Optical microscopy images were obtained from a BA310MET, Motic under ambient conditions (~22 °C and ~50% RH).

The pH was measured by a portable pH/mV/°C meter (HI 8424, HANNA), and the capsule unit was calibrated in pH 1, 4, and 7 buffer solutions maintained at 23 °C. The hydrodynamic radius (R_h), zeta potential, and solution ionic conductivity of PEDOT:PSS nanoparticles in suspension were measured using dynamic light scattering (DLS) spectra with a Zetasizer Nano ZS90 (Malvern Instruments, inc.). Then, 60 μL of an NPC solution (or PEDOT:PSS) was mixed with 5 mL of deionized water for dilution. A supernatant solution was stabilized in a cuvette for 12 h. Error bars reflect the standard deviation from ten identical measurements.

The thermal conductivity was determined from the specific heat capacitance and thermal diffusivity according to the equation $\kappa=C_p\,\alpha\,\rho$, where C_p is the specific heat capacitance, α is the thermal diffusivity, and ρ is the density of the sample. The C_p was measured by differential scanning calorimetry (DSC, 200 F3 Maia, NETZSCH) under N_2 gas flow at a heating rate of 10 °C min^{-1}. The α was measured by laser flash analysis (LFA) in a 25 °C chamber, and the value of pristine sample was checked against that obtained by LFA457, NETZCH. NPC solutions of 5 mL were dried at room temperature for 24 h to achieve a desired thickness of 0.5 mm.

The ion-transport number[5] is represented as

$$t_i = i_i/(i_i + i_e) \quad \text{(Equation S4)}$$

and the electron transference number is represented as

$$t_e = i_e/(i_i + i_e) \quad \text{(Equation S5)}$$

where i_i and i_e are their respective partial currents with $t_i + t_e = 1$.

In the ionic conductive polymer film, the heat is converted into the electrical energy and stored at the electrode of the capacitor. Thus, the stored electrochemical energy (E_{ch}, J) was determined by Equation S6:

$$E_{ch} = \frac{1}{2}CV_{th}^2 \quad \text{(Equation S6)}$$

where C is the capacitance (F) of the sample and V_{th} is the voltage induced by the ΔT.

Electron spin resonance (ESR) spectrometry was performed by Bruker (EMXplus-9.5/2.7). PEDOT:PSS doped with different concentrations of $CuCl_2$ were prepared by drop-casting method. Certain amount of these dopant was added to PEDOT:PSS solution to obtain the concentrations: 0, 14, 25, 40, and 57 wt %. The mixture was drop-casted to a PET film and kept at 50% RH and 343 K for 12 h. The thickness of these films was in the range of 30–40 μm. The doping level W (wt %) was calculated from the following equation:

$$W = \frac{W_d}{W_d + W_p} \quad \text{(Equation S7)}$$

where W_p and W_d represent the weight of polymer and dopant, respectively.

The proportionality factor (g-factor) was calculated from the following equation:

$$g = \frac{\mu_B B_0}{hv} \quad \text{(Equation S8)}$$

where h is the Planck constant, v is the microwave frequency (9.4 GHz), μ_B is the Bohr magneton, and B_0 is the magnetic field strength. The doping level dependence of NPC films was demonstrated with the number of spins (N), peak-to-peak separation (ΔH_{pp}) of the ESR

Lorentzian signal, asymmetry factor (A_1/A_2 the ratio between the two halves of the signal) and g-factor (Fig. S1).

Theoretical equations for ionic Seebeck voltage generation.

1. Grotthuss diffusion mechanism in conductivity

The calculated S values of the NPC films were obtained from the calculated V_{out} using the Grotthuss mechanism at a uniform gradient of temperature.[6, 7] The V_{out} at a small distance, *d*, for anion was calculated as Equation S9–S11:

$$|V_{out}| = \frac{qE_a d^2}{12\varepsilon_r\varepsilon_0 k_B T}\frac{\Delta T}{T}\nabla n \qquad \text{(Equation S9)}$$

$$|I_{sc}| = \frac{1}{R}\frac{qE_a d^2}{12\varepsilon_r\varepsilon_0 k_B T}\frac{\Delta T}{T}\nabla n \qquad \text{(Equation S10)}$$

$$|S| = \frac{qE_a d^2}{12\varepsilon_r\varepsilon_0 k_B T}\frac{1}{T}\nabla n \qquad \text{(Equation S11)}$$

where q is the electron charge, E_a is the activation energy of ions, ε_r is the relative permittivity, ε_0 is the vacuum permittivity, k_B is the Boltzmann constant, T is the average temperature within the distance d, and ∇n is the concentration gradient of ions. The V_{out} is proportional to n_0, therefore, NPC films with high $CuCl_2$ contents can show a large V_{out} and S value. The calculated V_{out} from Equation S9 was –25.5 and –80.2 mV for NPC14 and NPC40 (at $E_a = 0.03$ eV, d = 0.3 cm, ε_r = 10,000 and 8,000, $\Delta T = 4.5$ K, and $n_0 = 1.07–2.72 \times 10^{13}$ cm^{-3}), respectively, and these are well-agreed with experimental values (–24.8 and –81.9 mV). The calculated I_{sc} from Equation S10 was 49 and 270 nA for NPC14 and NPC40, respectively, and these are well-agreed with experimental values (47 and 270 nA). The calculated S from Equation S11 was –5.7 and –18.1 mV K^{-1} for NPC14 and NPC40, respectively, and these are well-agreed with experimental values (–5.5 and –18.2 mV K^{-1}).

$$|V_{oc}| = \frac{E_a d^2 \quad \Delta T}{24\lambda_{DH}^2 q \quad T} \qquad \text{(Equation S12)}$$

$$\lambda_{DH} = \sqrt{\frac{E_a d^2 \quad \Delta T}{24|V_{oc}|q \quad T}} \qquad \text{(Equation S13)}$$

In an electrolyte or a colloidal suspension, temperature derivatives consider the Debye length

$$\lambda_{DH}(T) = \sqrt{\varepsilon_r(T)\varepsilon_0 kT/(2q^2 n)} \qquad \text{(Equation S14)}$$

2. A charged 2D nanochannel immersed within an electrolyte solution (the electrical double layers (EDL) near the charged surface)[8-11]

$$S = S_Q + S_\psi = \frac{Q_+ - Q_-}{2eT} + \frac{\int_0^h \psi\cosh(\bar{\psi})dz}{T\int_0^h \cosh(\bar{\psi})dz} = \frac{1\,\Delta Q \int_0^h e^{-\bar{\psi}}dz - \frac{q}{2evn}}{T2ev \int_0^h \cosh(\bar{\psi})dy} + \frac{\int_0^h \psi\cosh(\bar{\psi})dz}{T\int_0^h \cosh(\bar{\psi})dz}$$

(Equation S15)

S_Q: the thermal generated electric field caused by the Soret-type thermophoretic ion motion

S: the thermal generated electric field induced by the EDL, which can be obtained by numerically solving the Poisson-Boltzmann equation beyond the Debye-Hückle linearization

$2h$: height

J±: the cationic and anionic ion fluxes

e is the electronic charge, kBT is the thermal energy, is the electrostatic potential

Q± is the heat of transport

The ion Fickian diffusion coefficients are $D\pm = \mu\pm\ kBT/e$, in which μ is the ion mobility

3. Soret coefficient for molecule[12, 13]

$$S_T = S_T^{(ionic)} + S_T^{(hyd)} = \frac{Q_{eff}^2 \lambda_{DH} \beta}{4A\varepsilon_r \varepsilon_0 kT^2} - \frac{As_{hyd}}{kT} = \frac{A}{kT}\left(- s_{hyd} + \frac{Q_{eff}^2 \beta}{4A\varepsilon_r \varepsilon_0 T} \times \lambda_{DH} \right)$$ (Equation S16)

In an electrolyte or a colloidal suspension, temperature derivatives consider the Debye length

$$\lambda_{DH}(T) = \sqrt{\varepsilon_r(T)\varepsilon_0 kT/(2q^2 n)}$$ (Equation S17)

a factor $\beta = 1 - \left(\frac{T}{\varepsilon_r}\right)\partial\varepsilon_r/\partial T$

A is the molecule area, Q_{eff} is the effective charge, and s_{hyd} is the particle-area-specific hydration entropy.

A thermal lens (TL) setup:

$$S_T = \frac{D_T}{D} = - \frac{1}{c(1-c)} \frac{\nabla c}{\nabla T}$$ (Equation S18)

$S_T = D_T/D$ is the Soret coefficient measured in K^{-1}, D_T is the thermal diffusion coefficient in $m^2\ s^{-1}\ K^{-1}$, D is the translational diffusion coefficient in $m^2\ s^{-1}$, and c is the weight fraction.

Table S1. Summary of impedance parameters and transport numbers obtained by fitting the electrochemical impedance spectroscopy.

Sample	RH%	C_{geo}[a] (F)	Z_{e}[b] (Ohm)	Z_{i}[c] (Ohm)	t_{e}[d]	t_{i}[e]
PEDOT:PSS	60	9.74×10^{-12}	6×10^{5}	8955	0.99	0.01
	70	1.75×10^{-11}	5×10^{5}	4364	0.99	0.01
	80	2.67×10^{-11}	4×10^{5}	2185	0.99	0.01
NPC14	60	9.34×10^{-12}	4.9×10^{6}	19251	1.00	0.00
	70	1.35×10^{-11}	706,420	7808	0.99	0.01
	80	2.01×10^{-11}	1.06×10^{6}	3339	1.00	0.00
NPC25	60	8.15×10^{-12}	2.61×10^{5}	20502	0.93	0.07
	70	1.13×10^{-11}	110,710	8355	0.93	0.07
	80	2.08×10^{-11}	102,260	3190	0.97	0.03
NPC40	60	1.24×10^{-11}	33,367	9489	0.78	0.22
	70	1.74×10^{-11}	20,708	5002	0.81	0.19
	80	2.48×10^{-11}	43,889	2467	0.95	0.05
NPC46	80	5.76×10^{-11}	152,290	816.7	0.99	0.01
NPC57	60	1.16×10^{-10}	19,553	489.9	0.98	0.02
	70	1.49×10^{-10}	12,013	382.3	0.97	0.03
	80	1.74×10^{-10}	15,615	302.2	0.98	0.02

[a]The geometrical capacitance, [b]the electrical, and [c]the ionic impedance calculated of the films from the simulated impedance spectrum. [d]The ionic and [e]the electric transport number according to Equation S4 and S5.

Figures and Legends

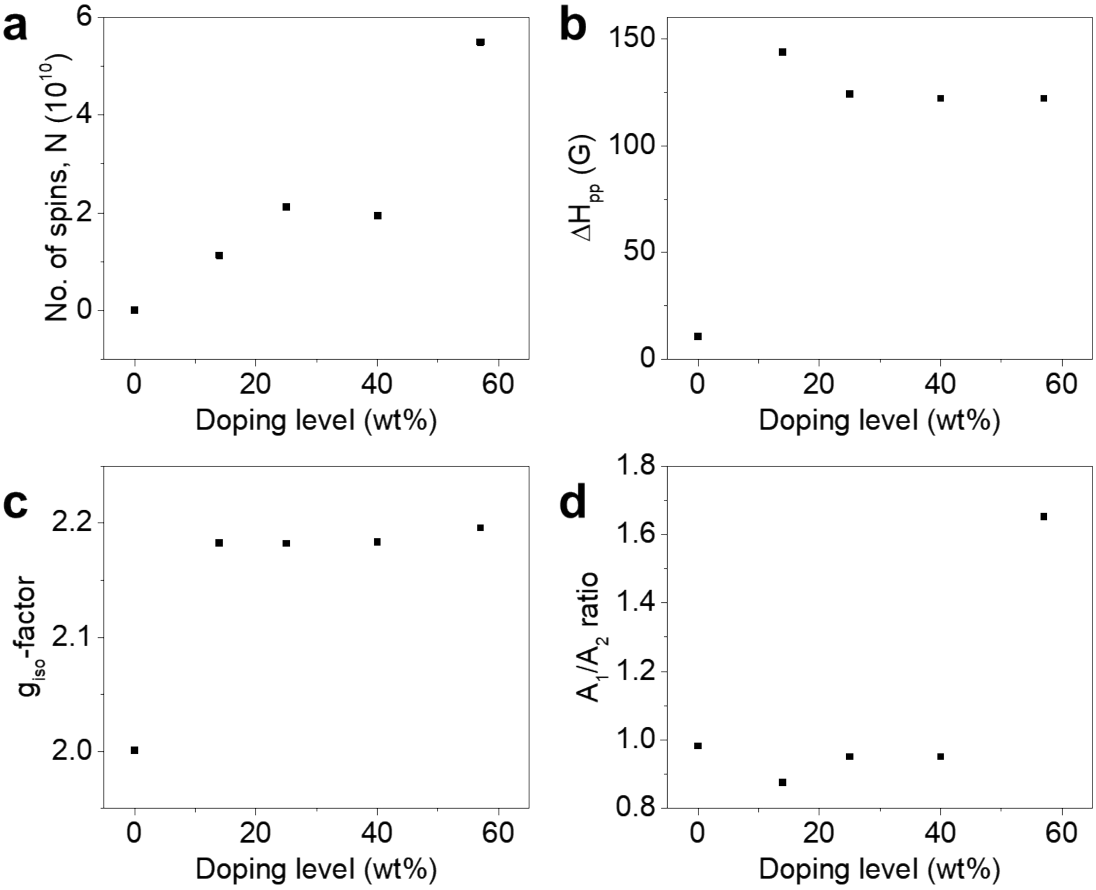

Fig. S1. Doping level dependence of ESR factors.

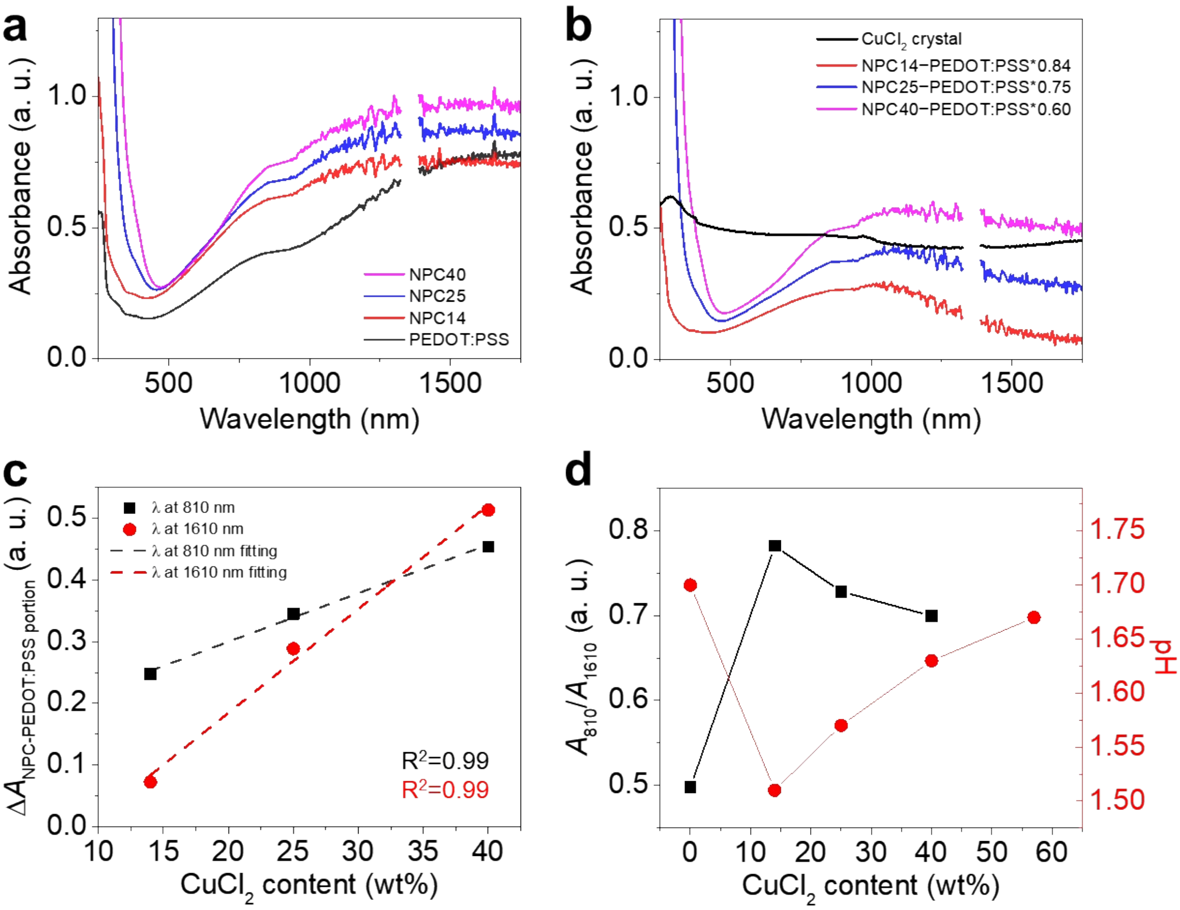

Fig. S2. (a) UV-vis-NIR spectrum of the PEDOT:PSS and NPC films with different $CuCl_2$ contents. (b) UV-vis-NIR spectrum of the NPC films excluding the absorbance corresponding to the content of $CuCl_2$. (c) Absorbance intensity difference (ΔA) at 1610 and 810 nm for the spectrum in (b). (d) Effect of $CuCl_2$ content of the corresponding absorbance ratio A_{810}/A_{1610} and pH of the films.

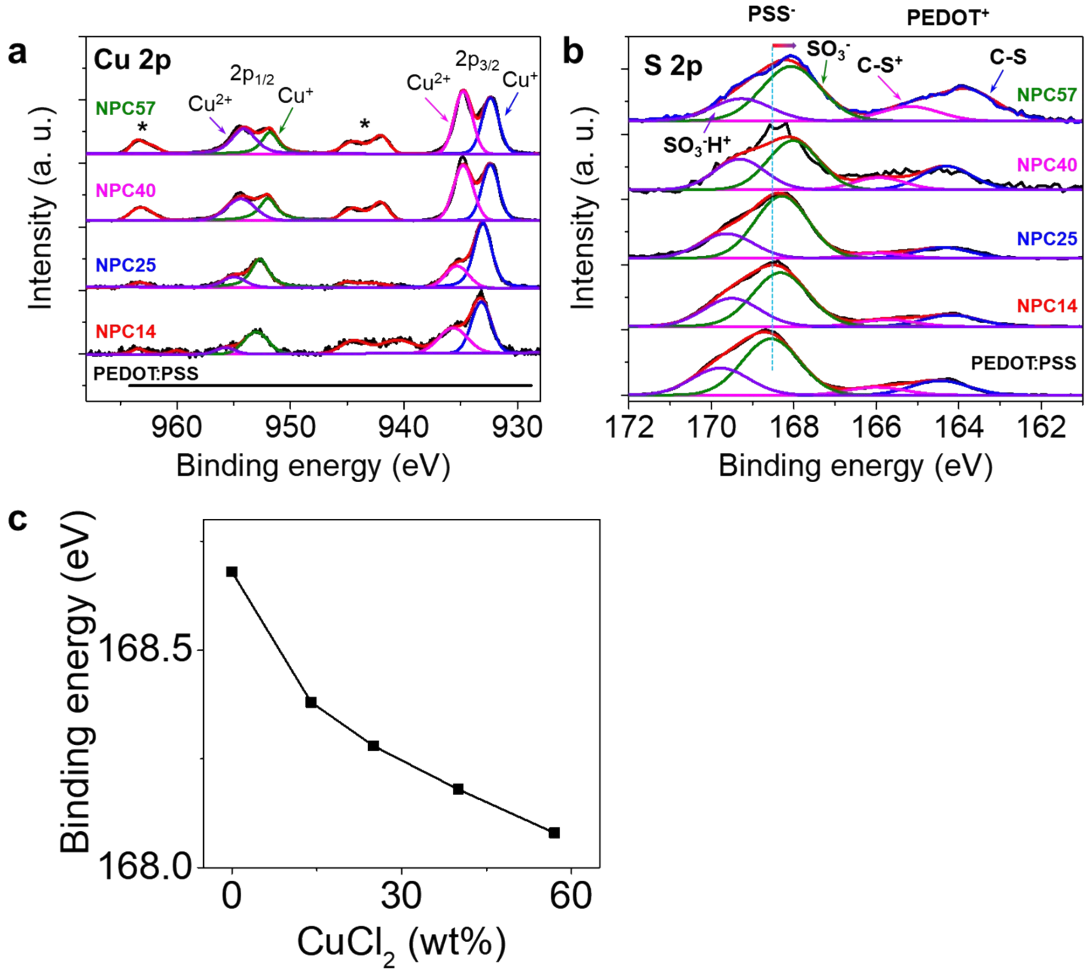

Fig. S3. High-resolution (a) Cu 2p and (b) S 2p photoelectron spectra of the NPC films. The Cu 2p spectrum was fit into four peaks, as evidenced by deconvolution, with the exception of shake-up satellites peaks. (c) The binding energy peak shift of PSS^{-} corresponding to the CuCl$_2$ wt%.

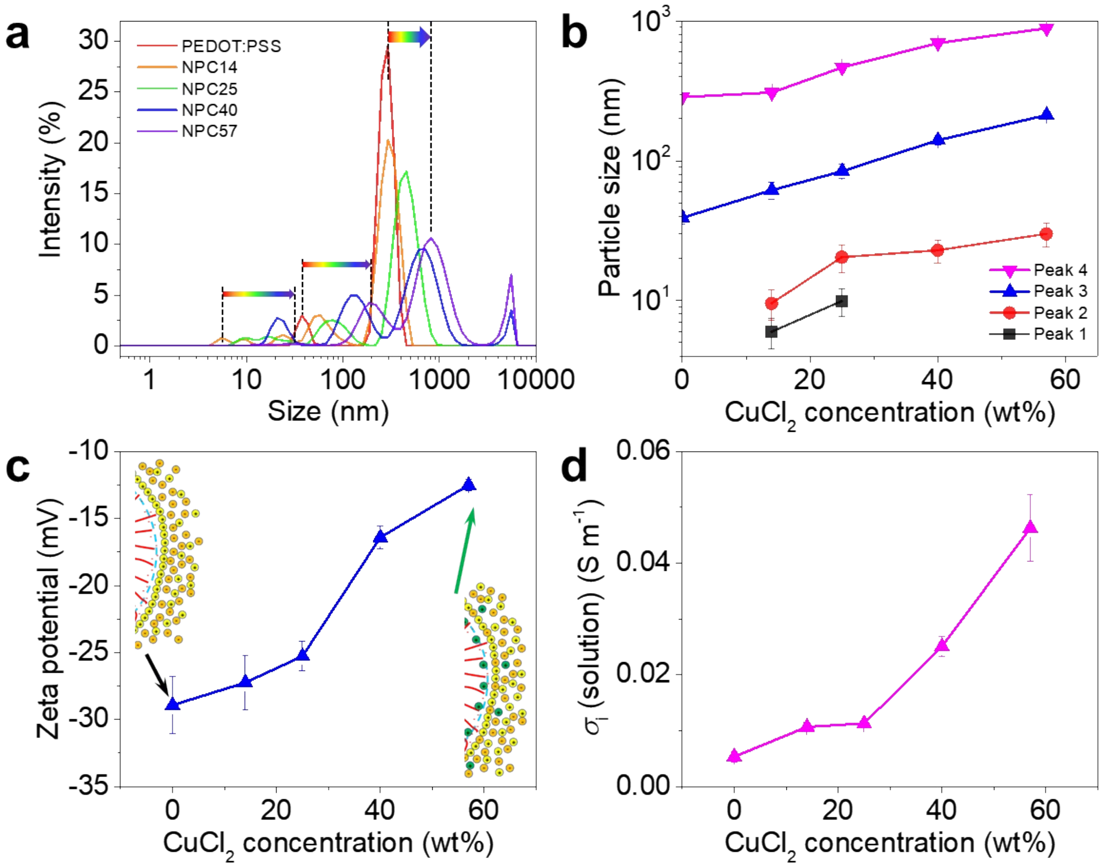

Fig. S4. (a) Size distribution of diluted NPC solutions by a dynamic laser scattering (DLS). (b) Hydrodynamic radius (R_h) of dilute NPC microgels for various $CuCl_2$ concentrations. (c) Zeta potential and (d) solution ion conductivity of diluted NPC solutions with different $CuCl_2$ contents.

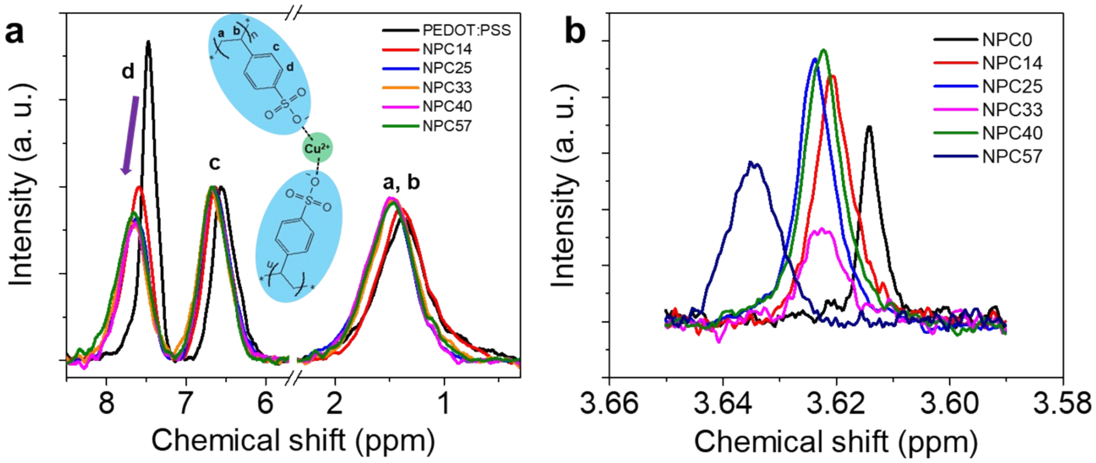

Fig. S5. Study of ionic cross-linking. ^{1}H NMR spectrum of (a) PSS and (b) PEDOT peaks of the diluted NPC solution in D_2O.

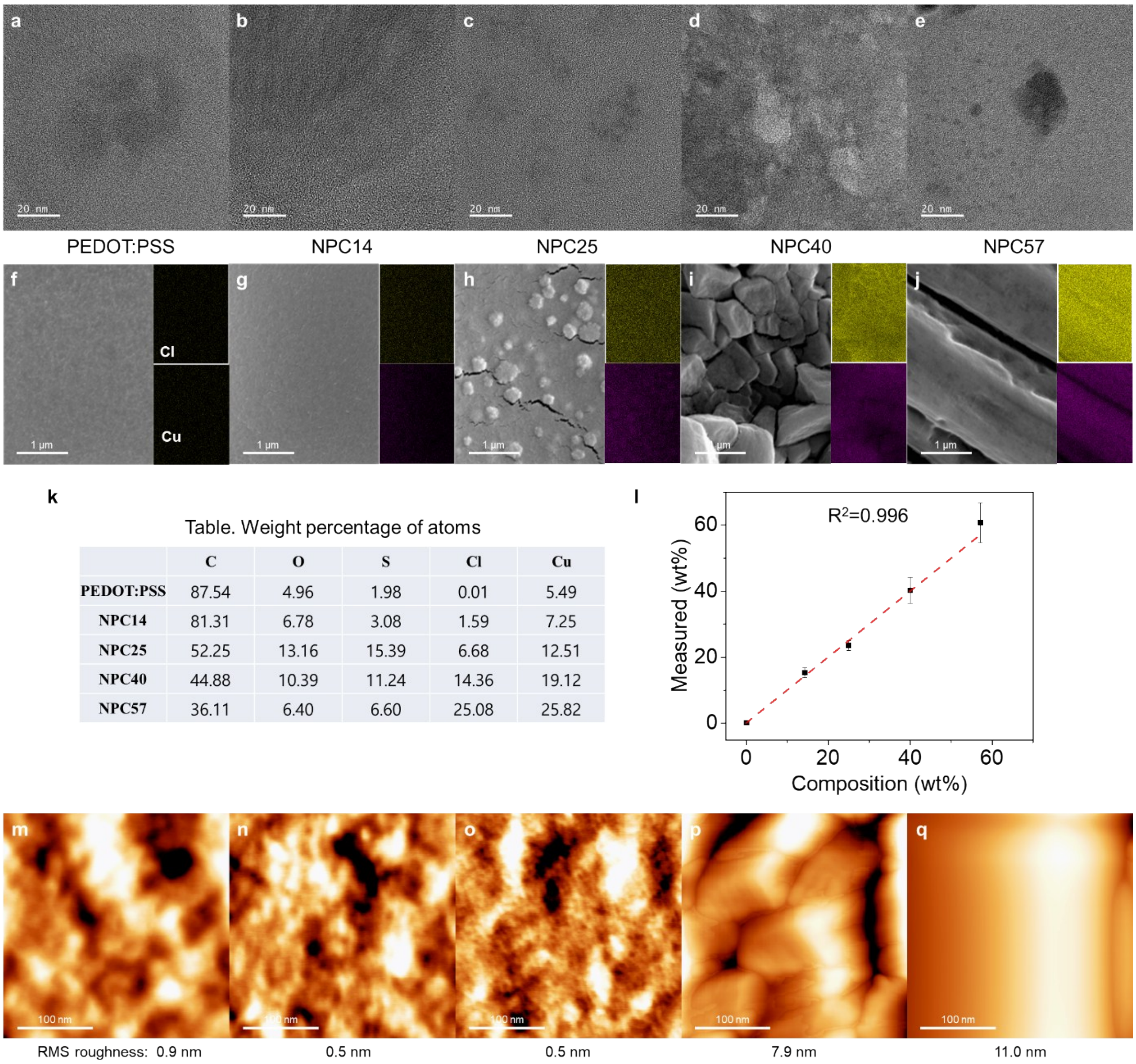

Table. Weight percentage of atoms

	C	O	S	Cl	Cu
PEDOT:PSS	87.54	4.96	1.98	0.01	5.49
NPC14	81.31	6.78	3.08	1.59	7.25
NPC25	52.25	13.16	15.39	6.68	12.51
NPC40	44.88	10.39	11.24	14.36	19.12
NPC57	36.11	6.40	6.60	25.08	25.82

Fig. S6. (a-e) TEM images of the NPC films. The inset shows the electron diffraction pattern. (f-j) SEM and EDS mapping (Cl and Cu atoms) images and (k) EDS analysis table and (l) wt% of $CuCl_2$ content from mixture and EDS analysis. (m-q) AFM images of the NPC films.

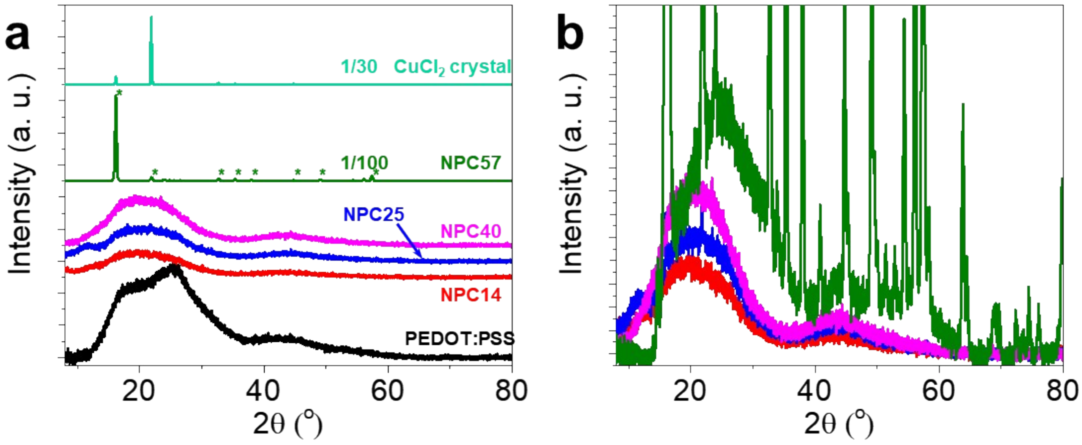

Fig. S7. XRD pattern of the films. (a) Re-scaled spectra and (b) narrow y-axis spectra. Sharp peaks of NPC57 and $CuCl_2$ crystal are characteristic XRD peaks of $CuCl_2 \cdot 2H_2O$.

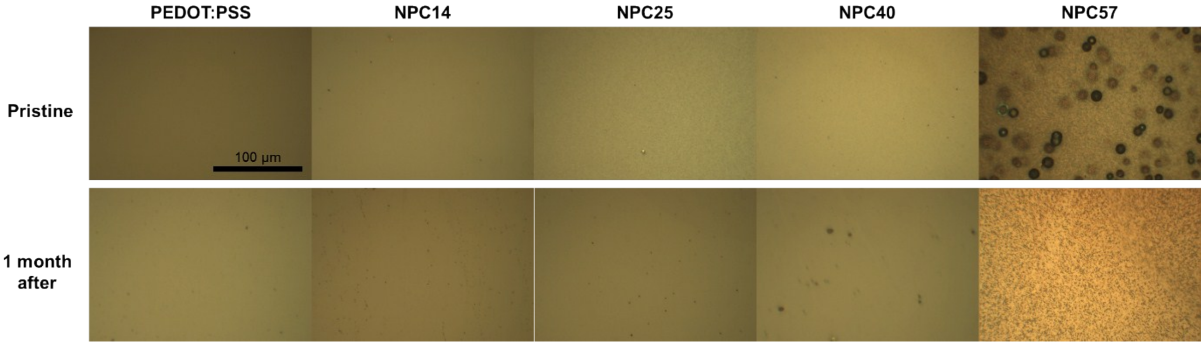

Fig. S8. Optical microscope images of the films with 50 times magnification stored at 50% RH and 25 °C.

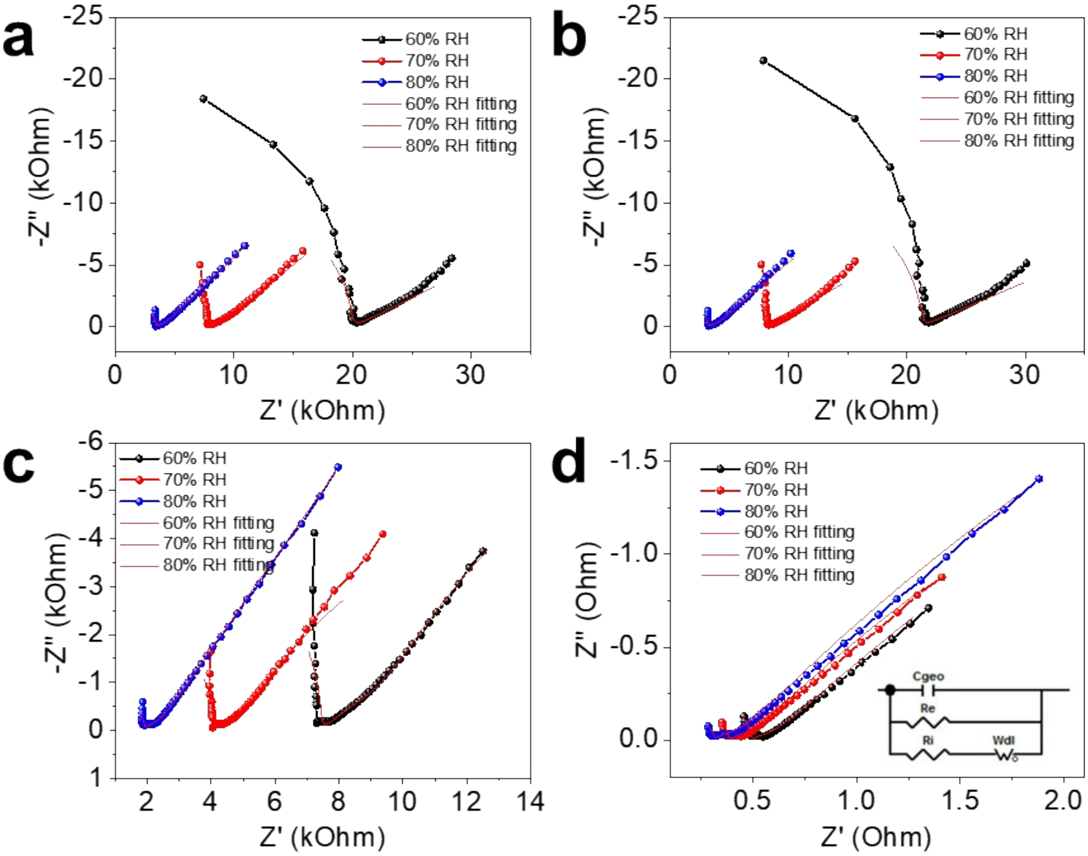

Fig. S9. Nyquist plots of (a) NPC14, (b) NPC25, (c) NPC40, and (d) NPC57 at an alternating voltage of 0.1 V and various humidity levels under frequencies ranging from 0.1 Hz to 0.8 MHz. Their equivalent circuit fittings are in the plot. (inset) The equivalent circuit model for obtaining each element in (d).[7]

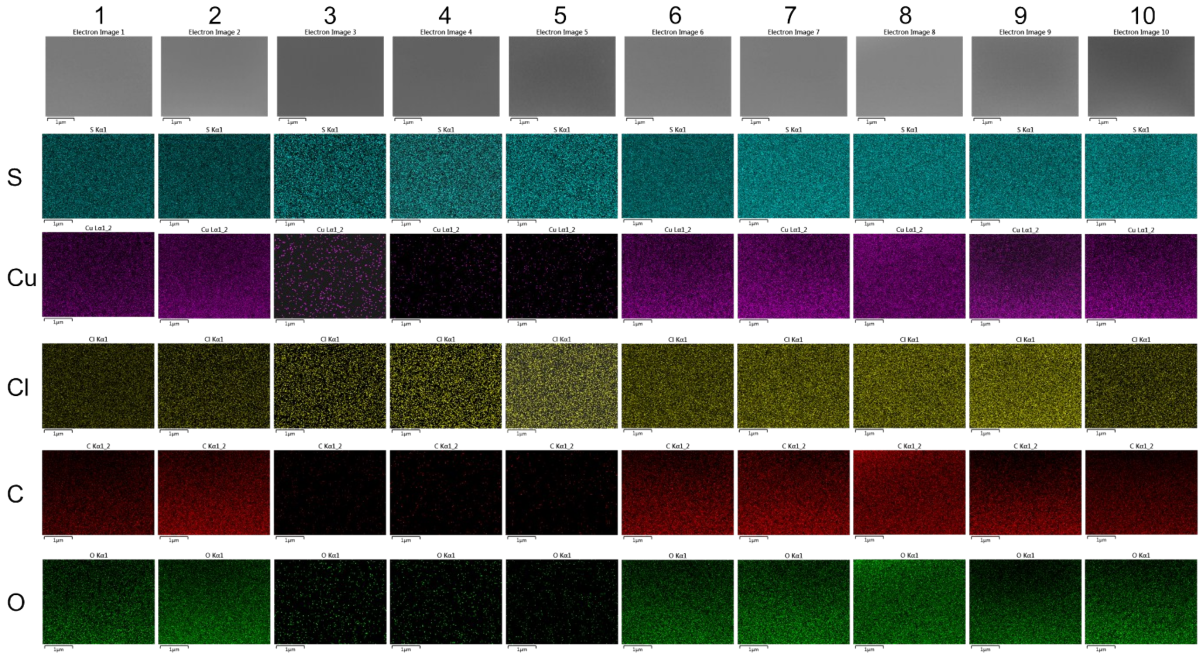

Fig. S10. SEM-EDS images of the area from 1 to 10 in Figure 3a.

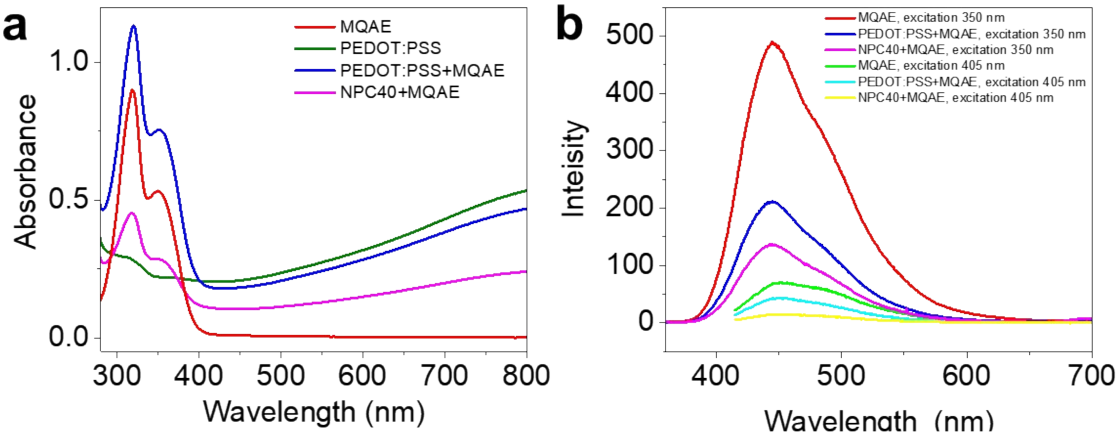

Fig. S11. (a) UV–vis absorbance of the MQAE-stained solution. (b) Fluorescence spectra of the MQAE-stained diluted solutions (0.0185 wt%) excited at 350 and 405 nm. Slit: 15/0 and 10/0 nm at 350 and 405 nm, respectively. Solid contents of MQAE was 0.5 wt%.

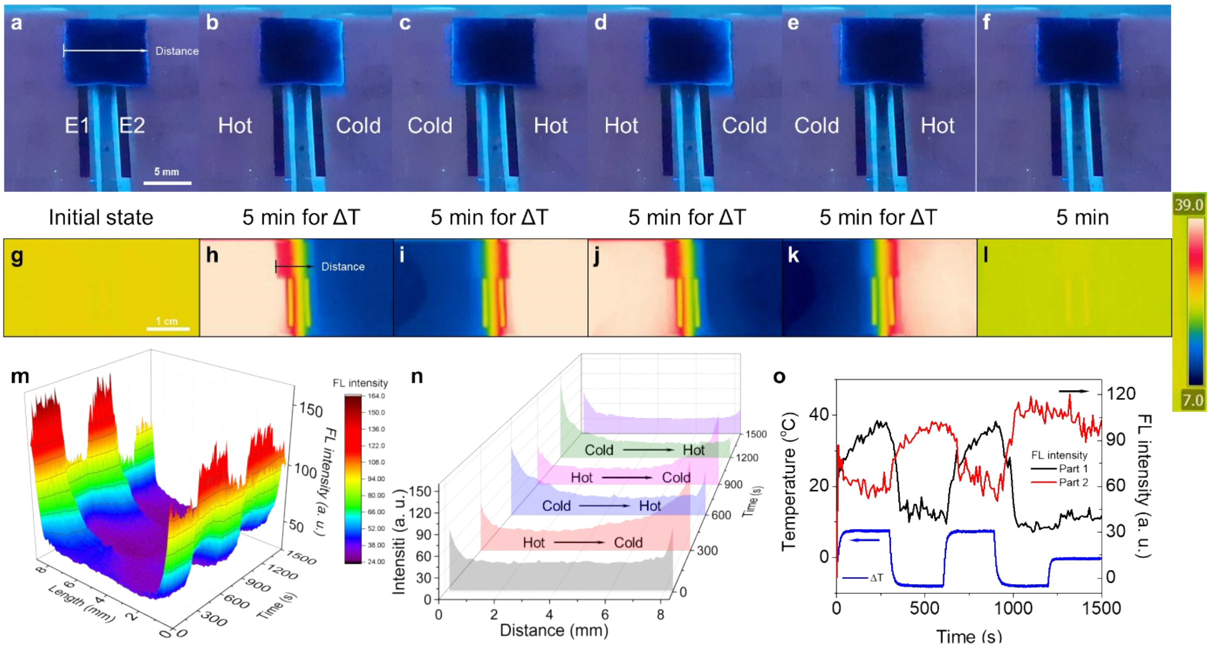

Fig. S12. Chlorine ion transport visualization. (a-e) A photograph of MQAE-stained NPC40 film on the gap of two Peltier devices. (a) Pristine film, (b) 5 min after heating–cooling, (c) 5 min after cooling–heating, (d) 5 min after heating–cooling, (e) 5 min after cooling–heating, (f) 5 min after ambient condition. (g-l) The corresponding IR images of a-f. (m) 3-D plot of the fluorescence intensity profile over time. (n) Fluorescence intensity profile of a-f. (o) Temperature and fluorescence intensity at two parts over time.

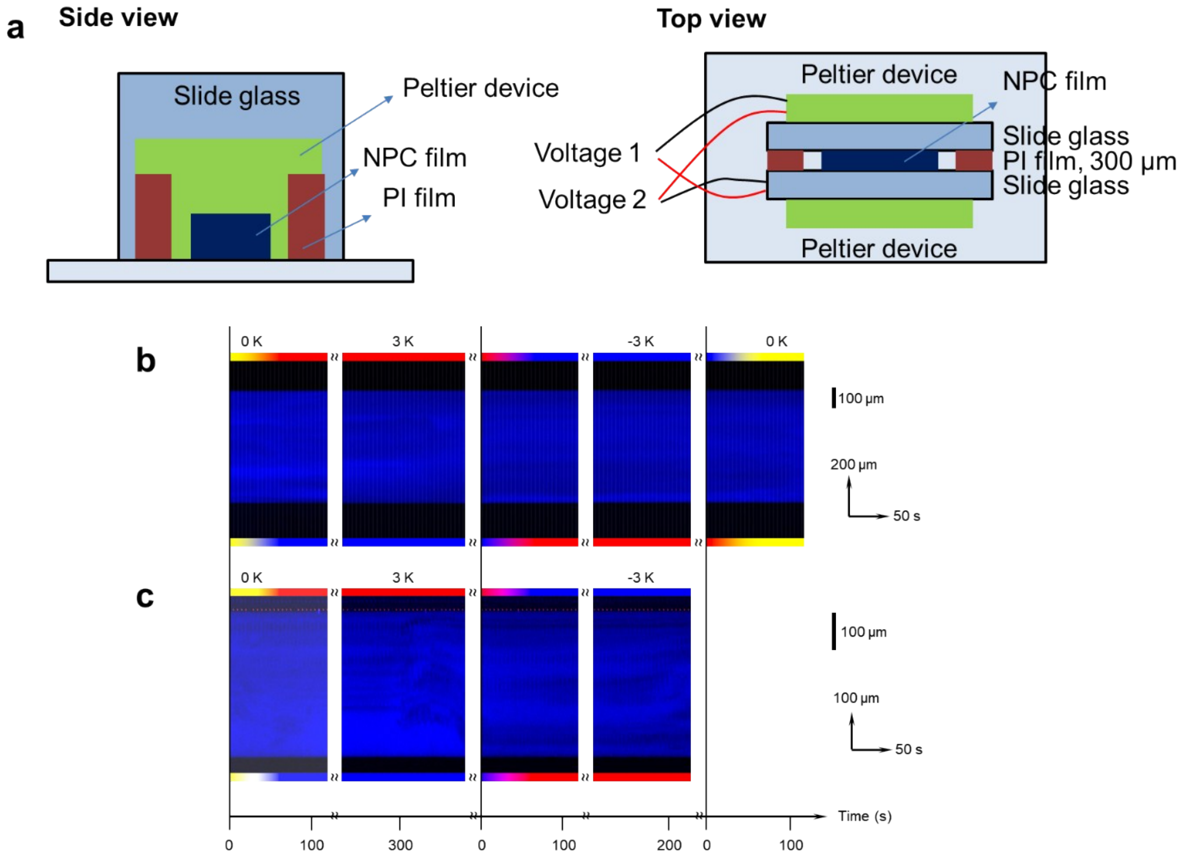

Fig. S13. In-situ fluorescence intensities between two slide glass visualized by analyzing the confocal microscopic intensities over time, for MQAE-stained PEDOT:PSS and NPC40 to trace the ion transport excited at 405 nm. (a) Side and top view of the setup. Stacked sliced images over time of (b) PEDOT:PSS and (c) NPC40 film with temperature gradient change.

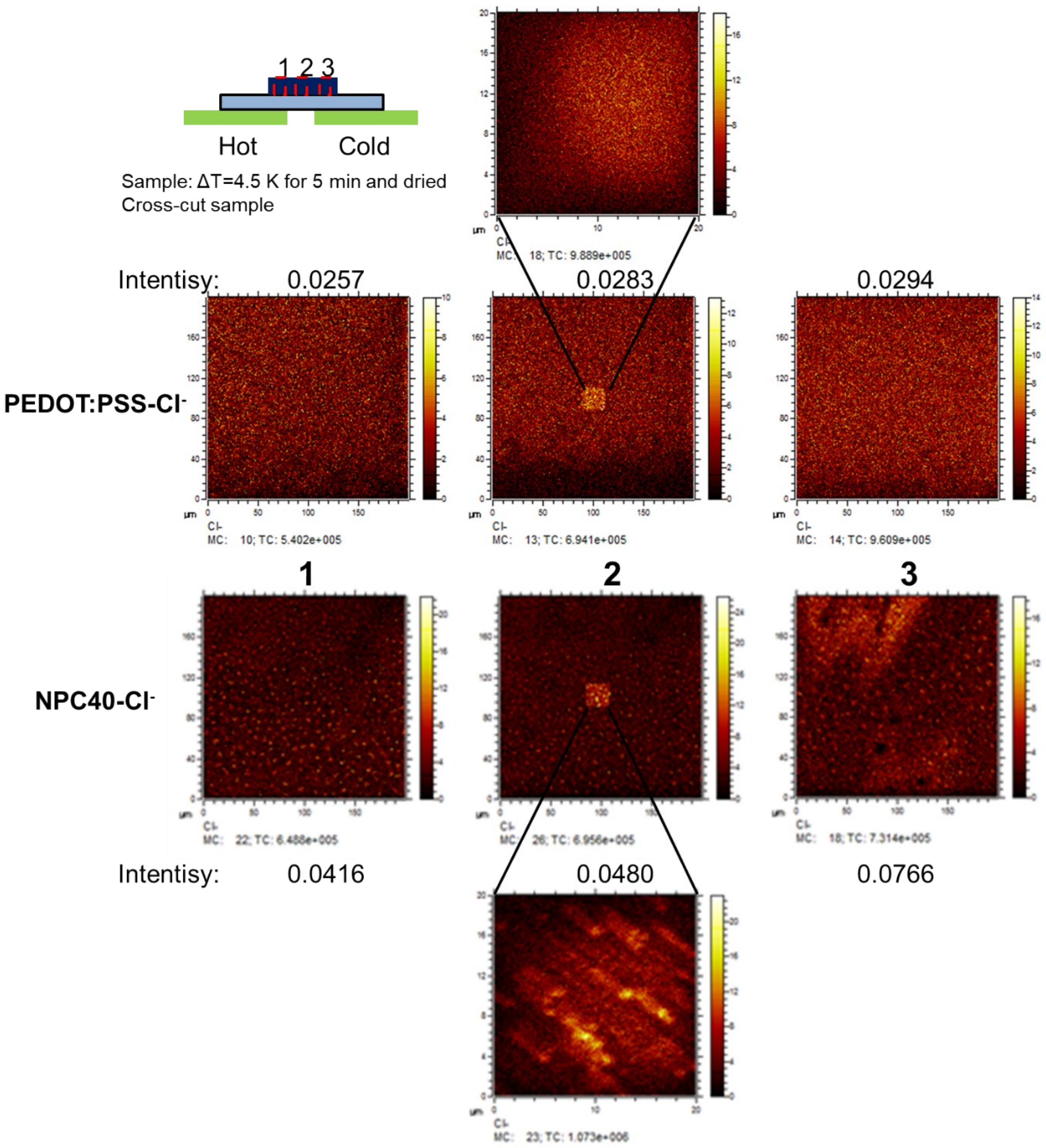

Fig. S14. ToF-SIMS images of PEDOT:PSS and NPC40 at area 1–3, respectively.

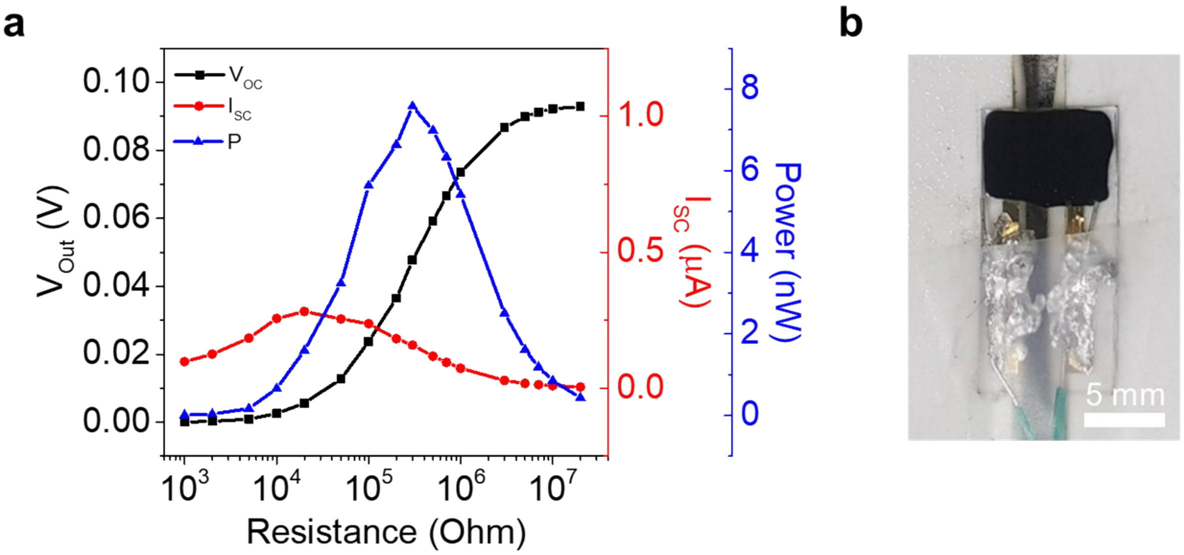

Fig. S15. (a) The variation of thermovoltage, current, and power of the NPC40 at 4.5 K and 80% RH with the external load resistance (R_{load}). (b) A photograph of the NPC40 device.

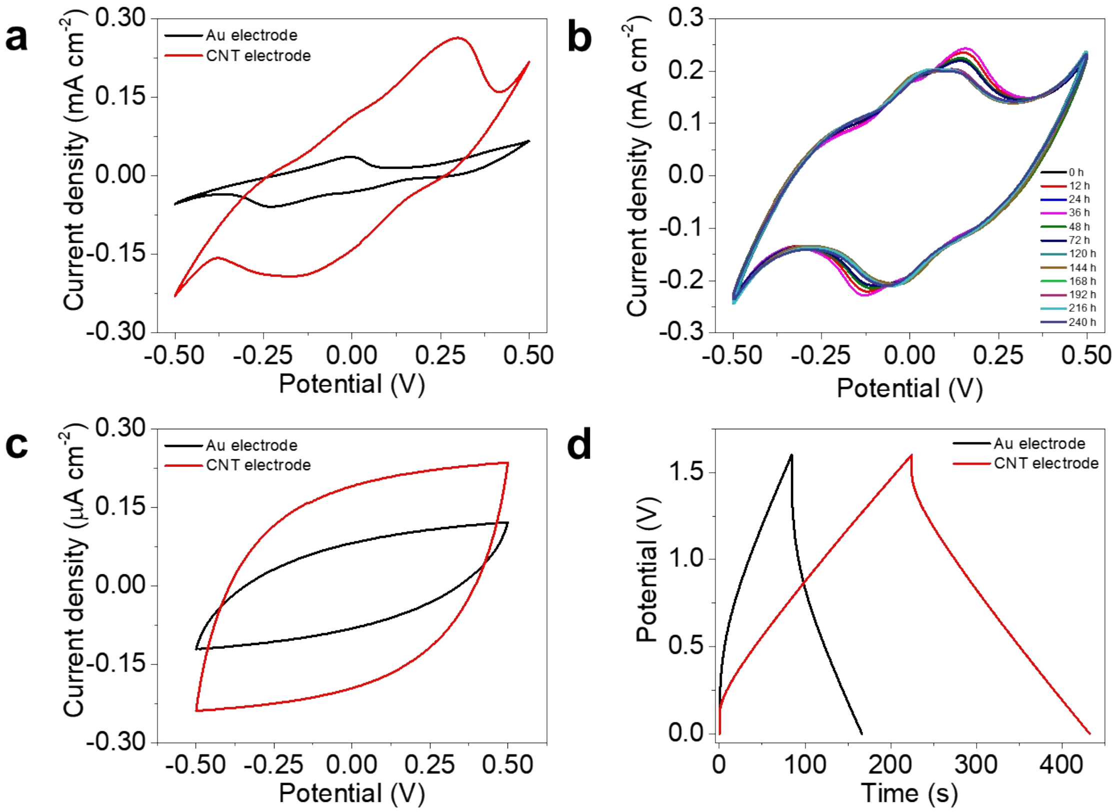

Fig. S16. The 2-electrode cyclic voltammograms for (a, b) NPC40 and (c) the flexible module-type TE harvester with 10 pairs of p-n legs on Au or CNT electrodes at 80% RH. (b) NPC40 film on the CNT electrode. (d) Galvanostatic charge-discharge curves of the flexible module-type TE harvester at 80% RH.

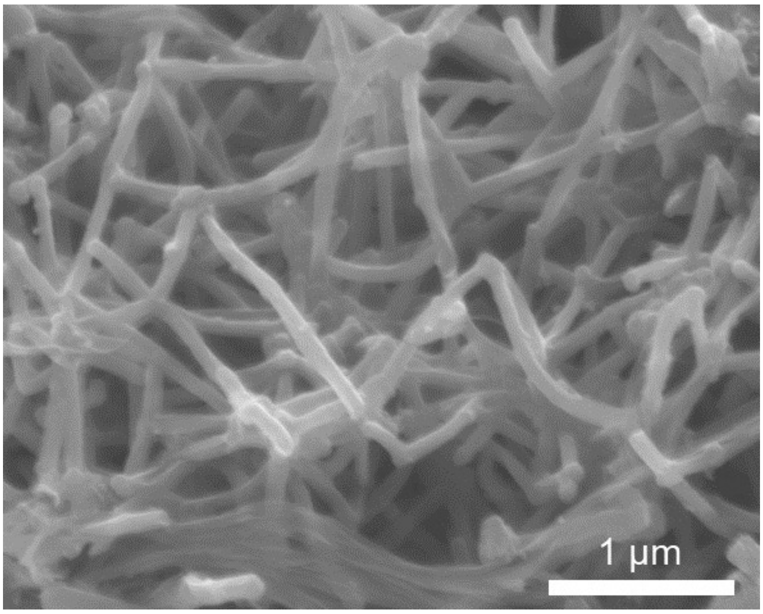

Fig. S17. An SEM image of the CNT electrode.

References

1. T. Kuner and G. J. Augustine, *Neuron*, 2000, **27**, 447-459.
2. I. Nuramdhani, M. Jose, P. Samyn, P. Adriaensens, B. Malengier, W. Deferme, G. De Mey and L. Van Langenhove, *Polymers*, 2019, **11**, 345.
3. T. Park, C. Park, B. Kim, H. Shin and E. Kim, *Energy & Environmental Science*, 2013, **6**, 788-792.
4. B. Kim, M. Han and E. Kim, *Journal of Materials Chemistry A*, 2019, **7**, 2066-2074.
5. R. A. Huggins, *Ionics*, 2002, **8**, 300-313.
6. M. A. Reznikov, *MRS Proceedings*, 2011, **1325**, mrss11-1325-e1307-1309.
7. B. Kim, J. Na, H. Lim, Y. Kim, J. Kim and E. Kim, *Adv. Funct. Mater.*, 2019, **29**, 1807549.
8. A. Würger, *Rep. Prog. Phys.*, 2010, **73**, 126601.
9. M. Dietzel and S. Hardt, *Phys. Rev. Lett.*, 2016, **116**, 225901.
10. A. L. Sehnem, D. Niether, S. Wiegand and A. M. Figueiredo Neto, *The Journal of Physical Chemistry B*, 2018, **122**, 4093-4100.
11. T. Li, X. Zhang, S. D. Lacey, R. Mi, X. Zhao, F. Jiang, J. Song, Z. Liu, G. Chen, J. Dai, Y. Yao, S. Das, R. Yang, R. M. Briber and L. Hu, *Nat. Mater.*, 2019, **18**, 608-613.
12. S. Duhr and D. Braun, *Proceedings of the National Academy of Sciences*, 2006, **103**, 19678-19682.
13. P. Polyakov and S. Wiegand, *PCCP*, 2009, **11**, 864-871.